

# An Original Way of Using COMSOL® Application Builder to Enhance Multiphysical Simulation of Laser Welding Processes

Y. A. Mayi<sup>1,2,\*</sup>, M. Dal<sup>2</sup>, P. Peyre<sup>2</sup>, M. Bellet<sup>3</sup>, C. Metton<sup>1</sup>, C. Moriconi<sup>1</sup>, R. Fabbro<sup>2</sup>

1. Safran Additive Manufacturing, a technology platform of Safran Tech, Rue des Jeunes Bois, Chateaufort, 78114 Magny-Les-Hameaux, France

2. Laboratoire PIMM, Arts et Metiers Institute of Technology, CNRS, Cnam, HESAM University, 151 boulevard de l'Hopital, 75013 Paris, France

3. MINES ParisTech, PSL Research University, CEMEF – Centre de Mise en Forme des Matériaux, CNRS UMR 7635, CS10207 rue Claude Daunesse, 06904 Sophia Antipolis, France

## Abstract

The present work introduces an innovative methodology, based on COMSOL® Application Builder, to account for the “beam trapping” effect in multiphysical modelling of laser welding. This phenomenon is known to be determinant to keyhole dynamics and stability. The method is rather simple. On one hand, there is a keyhole model based on the Arbitrary Lagrangian Eulerian (ALE) method, which computes heat transfer and fluid flow within the melt pool. On the other hand, there is a laser beam model, based on ray-optics description, which computes the absorbed laser flux in accordance with the keyhole geometry. Both models are run sequentially via a JAVA® method, so the laser heat source is updated self consistently as the keyhole forms, deforms and fluctuates. Despite its simplicity, the method is quite efficient and allows simulating transient keyhole formation in accordance with most recent dynamic x-ray images available in the literature.

## Keywords

COMSOL Multiphysics®, Application Builder, JAVA® methods, laser welding, Laser Powder Bed Fusion (LPBF), keyhole, beam trapping, multiple reflections.

## 1. Introduction

The need for high-fidelity multiphysical models in thermal laser processes increases, especially for Laser Powder Bed Fusion (LPBF) which became a popular additive manufacturing process. These numerical tools are attractive as they offer diagnostic capabilities on local physical phenomena that are difficult or expensive to get with experiments. One of those is the “beam trapping” effect (Figure 1). When the melt pool depression induced by recoil pressure reaches a critical aspect ratio, the incident laser irradiation gets “trapped” by multiple

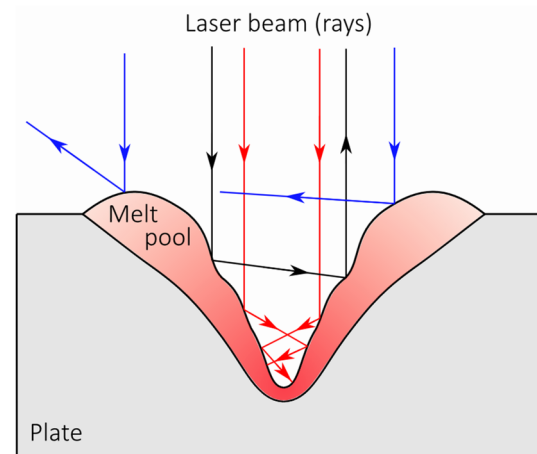


Figure 1 Illustration of the “beam trapping” phenomenon.

absorptions. This defines the keyhole mode. As a result, the keyhole absorptance increases but the melt pool becomes unstable as the incident laser power is absorbed heterogeneously on the keyhole walls. Early researchers, such as Ki et al. [1] and Lee et al. [2], have included this phenomenon in their numerical model, often thanks to a Ray-Tracing (RT) algorithm. Since then, several authors have published similar models, whether in spot welding [3, 4], welding [5–7] or LPBF [8, 9] configuration.

In the COMSOL® community, some works were also dedicated to multiphysical simulation of laser-material interaction, but they rarely accounted for laser beam trapping. For instance, Courtois et al. [10] developed the first self-consistent model of laser beam trapping in COMSOL® environment. Laser irradiation was treated as an electromagnetic problem, and stationary Maxwell’s laws were solved together with transient heat, fluid flow and Level-Set equations. However, the approach was quite computationally expensive and limited to pulsed laser welding with 2D axisymmetric assumption. Then, Tomashchuk et al. [11] presented a model of dissimilar laser welding, based on the ALE

\* Corresponding author: yaasin.mayi@safrangroup.com (Yaasin. A. Mayi)

approach, but with a constant absorption coefficient. Later, Bruyere et al. [12] developed a phase-field model of pulsed laser welding. They adjusted the keyhole absorptance using the Gouffé law [13] – which computes the absorptance of an irradiated cavity according to its geometry – to match final dimensions of experimental melted zones. But this approach excluded any discussion on transient keyhole formation and instabilities that may lead to defects. We have also contributed to the literature [14], with an ALE model of stationary laser irradiation with validated metal vapour velocities, but for melt pools of low aspect ratio.

In summary, there is to date no operational method implemented in COMSOL Multiphysics®, able to produce detailed description of transient keyhole formation in static and scanning laser configurations. Therefore, a clear need to enrich COMSOL® modelling experience has been identified here. The current work precisely proposes a new modelling method, which gives COMSOL® users the opportunity to get a deeper insight on transient welding phenomena. The structure of the paper is as follow. First, the methodology and its underlying assumptions are introduced. Then, the governing equations together with the implemented physical properties, numerical constants and setup are presented. Thereafter, some results are investigated, starting with keyhole formation steps in stationary illumination, followed by a sensitivity analysis on key parameters and by an example of application to laser welding. Finally, a conclusion is drawn with emphasis on benefits, outlook, and possible improvements of the new method.

## 2. Methodology

The methodology proceeds as follows [Figure 2(a)].

Firstly, the laser welding model without ray tracing (referred to as “multiphysical problem”) is run [Figure 2(b)], until the maximum angle  $\Delta\alpha_{\max}$  at the metal/gas interface reaches a predefined threshold  $\alpha_{\text{th}}$ . At this point, the final time step  $t_{\text{stop}}$  is stored. The threshold angle  $\alpha_{\text{th}}$  corresponds to the inclination at which some “fresh” incident rays are reflected toward the melt pool for the first time. As first approximation  $\alpha_{\text{th}} \sim \pi/4$ , the value at which an incident ray is reflected horizontally. During this first step then, it is assumed that only the “fresh” rays contribute to the absorbed energy.

Then, the final coordinates of the metal/gas interface are used as initial geometry of the ray-optics study [Figure 2(c)], during which the absorbed intensity is updated, taking into account the contribution of the rays that have interacted more than once with the melt pool [Figure 2(d)]. When the ray-optics study stops,

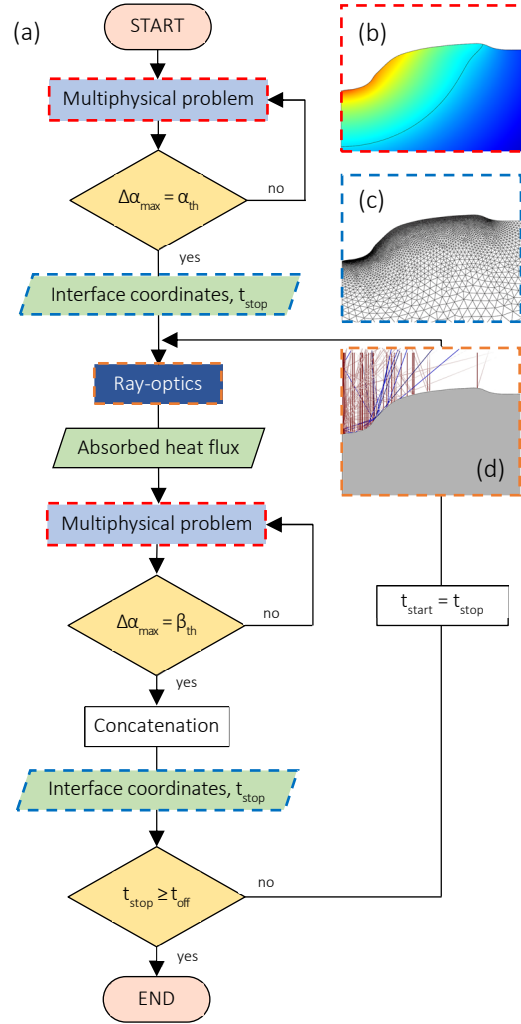


**Figure 2** Flowchart of the developed methodology.

the updated absorbed intensity is stored. As the time scale of the optics problem ( $< 1$  ns) is smaller than that of the multiphysical one ( $> 1$   $\mu\text{s}$ ) [10], it is justified to update the absorbed heat flux based on a “static” interface configuration.

Afterward, the new multiphysical study step is launched from  $t_{\text{stop}}$ , and with initial conditions the updated absorbed intensity and the final state of the first multiphysical study. This time, the problem stops when  $\Delta\alpha_{\max}$  reaches a second threshold  $\beta_{\text{th}}$ , of a few degrees. The choice of  $\beta_{\text{th}}$  determines the frequency with which the absorbed heat flux is updated. The smaller the threshold, the smaller the detectable variation in absorbed intensity. Usually, developers update the absorbed flux at predefined time steps, but here, we wanted to update it only when necessary, based on the state of the liquid/gas interface (at implicit events).

Finally, the solutions of the previous multiphysical problems are concatenated, and the second and third steps are repeated sequentially using a Do-While loop, until the final time step  $t_{\text{off}}$  is reached. The whole is programmed in JAVA® using the Application Builder.

### 3. Computational Model

#### 3.1. Ray-Optics

Using the Ray Optics module, the incident heat flux is modelled by a Gaussian law:

$$\vec{\varphi}_{\text{laser}} = \frac{2P}{\pi R_0^2} \exp\left(-2 \frac{r^2}{R_0^2}\right) \vec{k} \quad (1)$$

Where  $P$  and  $R_0$  are respectively the laser power and the  $1/e^2$  spot radius,  $r$  is the radial distance to the laser axis and  $\vec{k}$  is the direction of ray propagation.

At the first laser-material interaction, prior to any multiple reflections, the absorbed intensity  $I_{\text{abs}}^i$  is initialized analytically as:

$$I_{\text{abs}}^i = [1 - R_F] \vec{\varphi}_{\text{laser}} \cdot \vec{n} \quad (2)$$

Where  $R_F$  is the Fresnel reflectance and  $\vec{n}$  is the outer normal to the metal surface.

The reflectance  $R_F$  of the unpolarized laser beam can be calculated as a function of  $R_P$  and  $R_S$ , respectively the p- and s-polarized reflection coefficients [15]:

$$R_F = \frac{1}{2} (R_P + R_S) \quad (3)$$

$$R_P = \frac{[n - 1/\cos(\alpha)]^2 + k^2}{[n + 1/\cos(\alpha)]^2 + k^2} \quad (4)$$

$$R_S = \frac{[n - \cos(\alpha)]^2 + k^2}{[n + \cos(\alpha)]^2 + k^2} \quad (5)$$

Where  $n$  and  $k$  are the reflective indexes of the considered material, and  $\alpha$  is the laser incident angle.

However, here a constant reflectance  $R_F = R_0$  is implemented to perform a sensitivity analysis on this parameter. Physically speaking, this hypothesis is not too strong, because Fresnel reflectivity is involved in a range of depression aspect ratio that corresponds to a reflectance variation of a few percent only [16]. Absorption is then quickly dominated by multiple scattering.

Finally, the contribution of the multi-reflected rays is accounted for by:

$$I_{\text{abs}} = \sum_{\text{ray}=1}^{N_{\text{ray}}} \sum_{\text{refl}=1}^{N_{\text{refl}}} [1 - R_F(\alpha)] \vec{\varphi}_{\text{laser}} \cdot \vec{n} \quad (6)$$

Where  $N_{\text{ray}}$  is the number of rays and  $N_{\text{refl}}$  is the number of reflections per ray.

#### 3.2. Multiphysical Problem

The multiphysical problem aims to compute the melt pool hydrodynamics, driven by Laplace pressure (induced by surface tension), Marangoni shear stress (induced by temperature derivative of surface tension) and recoil pressure (induced by vaporisation).

The details of the model have already been published elsewhere [14], including at a previous COMSOL® conference [17]. Therefore, the main lines of the model are recalled here but for more details, please report to the dedicated papers.

Energy (7), mass (8) and momentum (9) conservation equations are solved using the CFD module:

$$\rho c_p^{\text{eq}} \frac{\partial T}{\partial t} + \rho c_p (\vec{u} \cdot \vec{\nabla} T) = \vec{\nabla} \cdot (k \vec{\nabla} T) \quad (7)$$

$$\vec{\nabla} \cdot \vec{u} = 0 \quad (8)$$

$$\rho \frac{\partial \vec{u}}{\partial t} + \rho (\vec{u} \cdot \vec{\nabla}) \vec{u} = \vec{\nabla} \cdot \left\{ -pI + \mu \left[ \vec{\nabla} \vec{u} + (\vec{\nabla} \vec{u})^T \right] \right\} + \vec{f}_v \quad (9)$$

At the metal/gas interface, laser input is counterbalanced by vaporization losses:

$$k \vec{\nabla} T \cdot (-\vec{n}) = I_{\text{abs}} - \dot{m} L_v \quad (9)$$

Where  $\dot{m}$  is the ablation rate [18].

Laplace pressure, Marangoni shear stress and recoil pressure are imposed at the liquid/gas boundary:

$$\left( -pI + \mu \left[ \vec{\nabla} \vec{u} + (\vec{\nabla} \vec{u})^T \right] \right) \cdot \vec{n} = -P_{\text{recoil}} \cdot \vec{n} + \sigma \kappa \vec{n} + \frac{\partial \sigma}{\partial T} \vec{\nabla}_s T \quad (10)$$

Where  $\kappa$  is the liquid/gas interface curvature.

The recoil pressure  $P_{\text{recoil}}$  can be approximated to:

$$P_{\text{recoil}} \sim \frac{1}{2} (1 + \beta_R) P_{\text{atm}} \exp \left[ \frac{ML_v}{RT_v} \left( 1 - \frac{T_v}{T} \right) \right] \quad (10)$$

Where  $P_{\text{atm}}$  is the atmospheric pressure.

#### 3.3. Moving Mesh

The free surface problem is tackled using the ALE method. The interface is discretized into a conformed mesh and its vertices follow the fluid movement according to:

$$V_i = \vec{u} \cdot \vec{n} \quad (11)$$

Where  $V_i$  is the velocity of the interface.

Interface displacement is then propagated through the domain, following the so-called Yeoh method [19] to ensure a smooth mesh deformation.

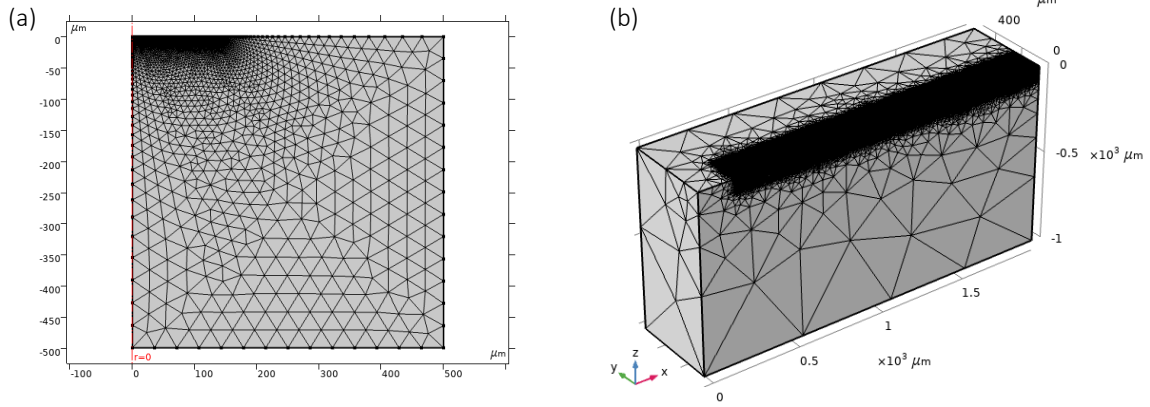


**Figure 3** (a) Mesh of 2D-axisymmetric domain. (b) Mesh of 3D domain.

### 3.4. Properties and Numerical Constants

Thermophysical properties considered in this study are those of Ti-6-Al-4V. Constant indicative values are given in Table 1, but full temperature-dependent properties are actually implemented in the model, using data compiled from ref. [18, 20–23].

### 3.5. Numerical Considerations

**3.5.1 Meshing** Two geometrical configurations are considered here. Firstly, the stationary laser study is solved assuming a cylindrical symmetry [Figure 3(a)]. In this case, the mesh is refined at the laser-material interaction zone (next to the symmetrical axis), down to  $1 \cdot 10^{-6}$  m. The total number of Degrees of Freedom (DOF) solved is about 50,000. Secondly, the laser welding study is solved assuming a symmetry plan at the intersection of the laser axis and the scan path [Figure 3(b)]. The mesh is refined all along the scan path and particularly at the laser-material interaction zone (down to  $3 \cdot 10^{-6}$  m). The corresponding number of DOF solved is about 600,000.

**Table 1** Properties used in the simulations.

Thermophysical properties (units)		values	ref.
$c_p$	Specific heat (J/kg/K)	740	[20]
$k$	Thermal conductivity (W/m/K)	26	[20]
$L_m$	Enthalpy of melting (J/kg)	$2.86 \cdot 10^5$	[20]
$L_v$	Enthalpy of vaporization (J/kg)	$8.90 \cdot 10^6$	[22]
$M$	Molar mass (g/mol)	0.0479	[20]
$R_0$	Reflectance	0.33	[21]
$T_{sol}$	Solidus temperature (K)	1878	[20]
$T_{liq}$	Liquidus temperature (K)	1923	[20]
$T_v$	Boiling temperature (K)	3558	[22]
$\beta_R$	Retro-diffusion coefficient	0.18	[18]
$\gamma$	Heat capacity ratio	1.67	-
$\mu$	Dynamic viscosity (Pa·s)	2.0	[20]
$\rho$	Density (kg/m <sup>3</sup> )	4200	[20]
$\sigma$	Surface tension (N/m)	1.38	[23]
$\partial\sigma/\partial T$	Thermocapillary coef. (N/m/K)	$-0.31 \cdot 10^{-3}$	[23]
Numerical constants			
$C_1/C_2$	Penalization constants	$10^6/10^{-5}$	-
$N_{ray}$	Number of rays	50,000	-
$\alpha_{th}/\beta_{th}$	Inclination thresholds (deg.)	35/10	-

**3.5.2 Solver setup** The multiphysical problem is solved in fully coupled approach using the direct PARDISO solver. Time step is set to  $1 \cdot 10^{-6}$  s, using the Backward Euler temporal scheme (first-order BDF) and the pre-implemented adaptive time stepping algorithm. The predefined solver configuration is used for the optical problem, with GMRES iterative solver and generalized-alpha temporal scheme.

## 4. Results and Discussion

### 4.1. Keyhole Dynamics in Laser Spot Welding

Figure 4(a)-(d) present the dynamic of keyhole formation in stationary laser mode, with a laser power of 156 W and a  $1/e^2$  spot size of 140  $\mu$ m. Here four steps are represented, with excellent agreement in comparison to recent state-of-the-art x-ray images [24]. First, after the laser is turned on, the irradiated material starts to melt in conduction regime [Figure 4(a)]. Then, when the boiling temperature is reached, the recoil pressure is exerted onto the melt pool and the vapour depression starts to deepen [Figure 4(b)]. During these first two steps, laser irradiation is absorbed only once by the melt pool and is reflected outward the system. In fact, these two stages represent what is typically simulated in the literature when no RT algorithm is accounted for.

Figure 4(e) shows how the simulated keyhole depth evolves with time, without and with RT. In the first case, the vapour depression continues to deepen at a very stable rate. In the second case, instabilities arise from  $t \sim 700 \mu$ s to  $t \sim 1034 \mu$ s. The absorbed laser intensity is redistributed along the keyhole wall by multiple scattering [Figure 4(c)], and the melt pool becomes unstable under the action of the recoil pressure. Then, at  $t = 1037 \mu$ s, the incident rays are reflected not only horizontally, but also downward. The melt pool acts like a concave mirror which focuses the laser on its optical axis. At this point, the absorbed intensity at the center of the interaction zone increases by 20. As a result, the penetration rate dramatically

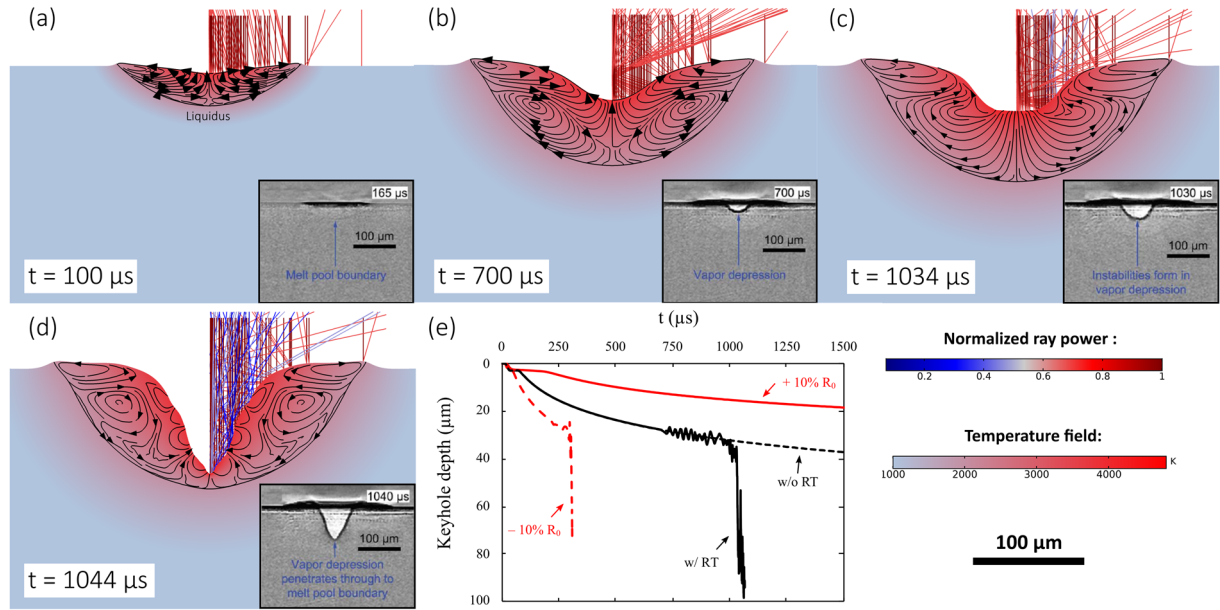


**Figure 4** (a)-(d) Simulated keyhole dynamics in static laser irradiation, compared to its experimental counterpart [24]. (e) Keyhole depth over time. The black line reports to the present simulation. The black dotted line refers to the same simulation without RT and the red lines represent the same simulation, with RT but with reflectance reduced and increased by 10% respectively.

increases and the depression switches instantaneously (in less than 10  $\mu\text{s}$ ) into a V-shape keyhole [Figure 4(d)]. This behaviour is in total agreement with recent x-rays observations [24] and, to the best of the author's knowledge, this is the first time that such threshold effect is shown by numerical simulation.

## 4.2. Sensitivity Analysis

**4.2.1. ...on reflectance  $R_0$**  Sensitivity analyses have been performed on two determinant parameters. The first one is the material reflectance  $R_0$ . Figure 4(e) shows how the keyhole depth over time evolves when  $R_0$  is reduced and increased by 10% respectively. The graph shows that  $R_0$  determines the penetration rate of the vapour depression, and thus the time at which the keyhole threshold is reached. When  $R_0$  is increased by 10%, the keyhole threshold is not reached within 1500  $\mu\text{s}$  of simulation. On contrary, when  $R_0$  is reduced by 10%, keyhole threshold is reached after 310  $\mu\text{s}$ , representing an underestimation of 70% compared to initial case.

Note that it is often difficult to know  $R_0$  with confidence. Here we have opted for a constant reflectance value supposedly valid on solid and liquid metal at any temperature. In fact,  $R_0$  depends on surface roughness, temperature, and does evolve with eventual formation of oxide layers. Hence, this result highlights how much experimental work on properties measurement are important, so that modelling effort can benefit reliable material data. Without such data, it is quite often necessary to calibrate reflectance to fit

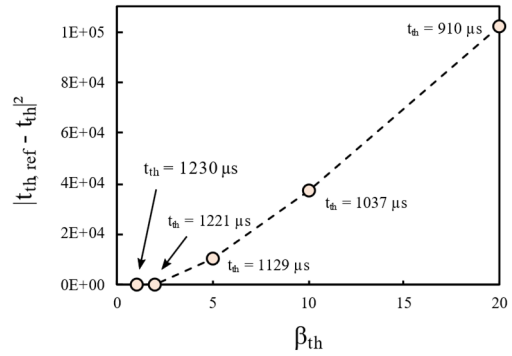


**Figure 5** Convergence graph of keyhole threshold time ( $t_{th,ref}$  is obtained with  $\beta_{th} = 1^\circ$ ).

experimental results. This is what we have done here, and this is also what did other authors, as Ye et al. [25] recently on the same alloy. Notice also that the present simulated case is a particular one, because the incident laser intensity is very close to the minimum intensity necessary to vaporize the alloy. At higher intensities, keyhole threshold is anyway reached relatively quickly, and absorption is then dominated by multiple scattering.

**4.2.2. ...on threshold angle  $\beta_{th}$**  We have also explored the influence of  $\beta_{th}$ , which determines the frequency with which the absorbed laser flux is updated. Contrary to  $R_0$ , the threshold angle  $\beta_{th}$  has no influence on the keyhole penetration rate, but only on the keyhole threshold time  $t_{th}$  (i.e. the time at which the vapour depression switches into a keyhole). In the previous simulation  $\beta_{th}$  was set to  $10^\circ$ , and the reflectance  $R_0$  was calibrated according to this value.

We have then launched four other simulations, with  $\beta_{th}$  taking the values of  $1^\circ$ ,  $2^\circ$ ,  $5^\circ$  and  $20^\circ$ , all things being equal. Figure 5 summarizes the results.

First note that,  $t_{th}$  increases when  $\beta_{th}$  decreases. This is actually not surprising, because with larger allowed angular amplitudes, the keyhole threshold is more easily overcome. Note also that the mean squared error  $|t_{th,ref} - t_{th}|^2$  (taking  $\beta_{th} = 1^\circ$  as reference) converges, meaning that a converged solution exists. Here this solution lies between  $1^\circ$  and  $2^\circ$ . Finally, notice that the error made in predicting  $t_{th}$  with large  $\beta_{th}$  is far less important than that made by taking incorrect value of  $R_0$ . Previously, when  $R_0$  was reduced by 10%,  $t_{th}$  was underestimated by 70%. Here, when the threshold angle is multiplied by 20,  $t_{th}$  is underestimated by 26% only. This result suggests that the importance of  $\beta_{th}$  may be relativized in comparison to  $R_0$ , especially because in many applications, it is not meaningful to predict  $t_{th}$  with an accuracy of  $100 \mu s$  (it is more meaningful to predict if keyholing is going to happen or not).

### 4.3. Example of Application to Laser Welding

Finally, we would like to demonstrate that the new method has been successfully applied to a 3D configuration. Figure 6 shows an application example to laser welding with laser power of 300 W, a  $1/e^2$  spot size of  $140 \mu m$  and a scanning speed of 700 mm/s. Keyhole dynamics in this configuration exhibits an evident similarity with the static case: we can found the

**Table 2** Calculation times with and without RT in static and scanning configurations.

	w/o RT	w/ RT
2D-axi	1 h	~ 1 week
3D	1-5 days	> 1 month

same conduction [Figure 6(a)], vapour depression [Figure 6(b)] and the keyhole steps [Figure 6(c)]. At steady state [Figure 6(d)], the predicted keyhole shape, with corrugations at the bottom and the rear of the liquid/gas interface, is in good agreement with experimental results performed with comparable process conditions [24].

However, it should be pointed out that this numerical performance comes at a cost. Table 2 compares the calculation times of the two previous configurations, with and without RT. These results were obtained using 8 cores of a workstation (CPU: Intel® Xeon Gold @3.1 GHz). Without RT, computational times are reasonable and quite compatible with industrial environment. The static case is computed within an hour and the scanning one in a few working days. The latter can even be simulated in a few hours with a coarser mesh. However, with RT, calculation time explodes, especially for the 3D configuration where steady state results are not expected in less than a month. Consequently, the new model method is well adapted to R&T environments where longer time spans are tolerated, but future work will be dedicated to extending its applicability.

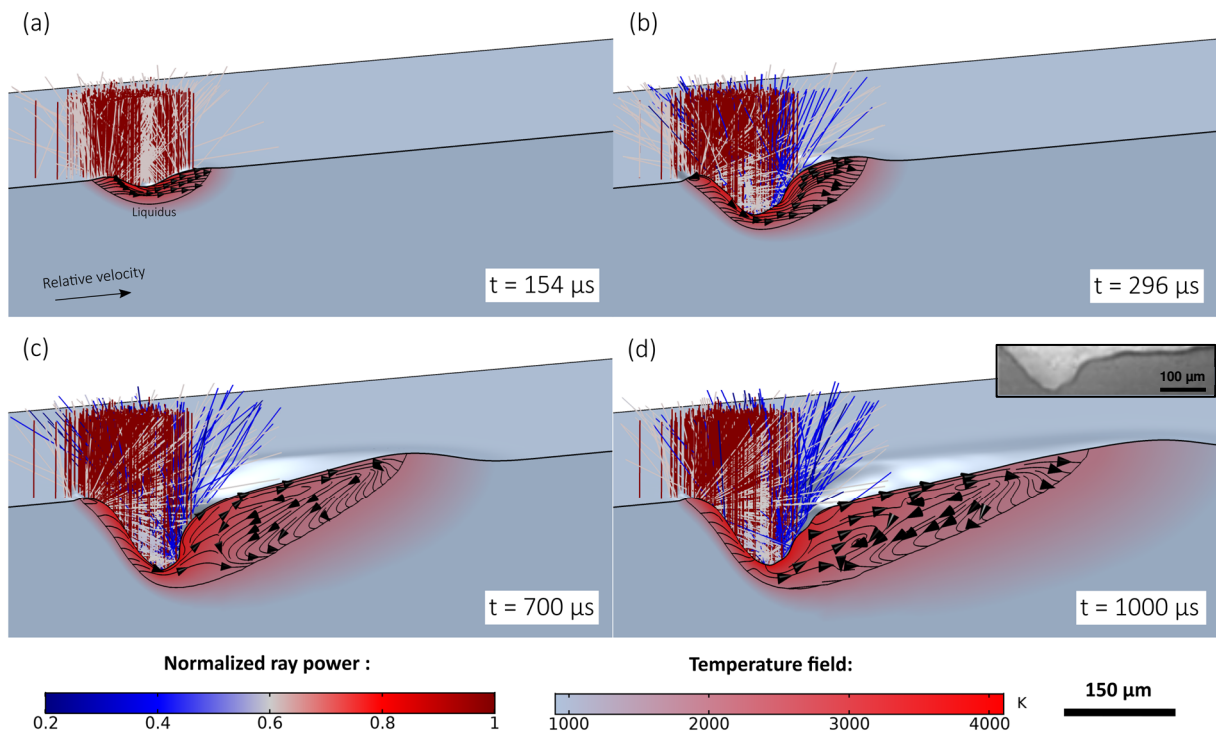


**Figure 6** Simulated keyhole dynamics in laser welding. X-ray image extracted from ref. [24].

## 5. Conclusions and Outlook

A new modelling method to account for the “beam trapping” effect in welding processes has been implemented in COMSOL®. This method is quite innovative as it involves two modules (CFD and Ray Optics) and requires advanced functionalities as implicit events, concatenation of solutions as well as development of a Java® method with the Application Builder. This approach has proven its ability to describe transient keyhole formation with high fidelity in pulsed laser welding as well as in laser welding.

Currently, the free surface problem is treated with the ALE method as the ray-material interaction is quite straightforward with this approach. However, note that the modelling method could be easily adapted to Eulerian interface tracking methods such as Level-Set or Phase-Field, with few additional developments. With a Eulerian description of the interface, it would be possible to investigate more unstable conditions (involving keyhole collapse and spatters), especially on highly reflective materials that are difficult to weld. A feasibility test has already been validated in our research group and new results will be presented soon.

## References

1. Ki, H., Mohanty, P.S., Mazumder, J.: Modelling of high-density laser-material interaction using fast level set method. *J. Phys. D: Appl. Phys.* 34, 364–372 (2001).
2. Lee, J.Y., *et al.*: Mechanism of keyhole formation and stability in stationary laser welding. *J. Phys. D: Appl. Phys.* 35, 1570–1576 (2002).
3. Medale, M., Touvrey, C., Fabbro, R.: An axisymmetric thermo-hydraulic model to better understand spot laser welding. *European Journal of Computational Mechanics.* 17, 795–806 (2008).
4. Tan, W., Bailey, N.S., Shin, Y.C.: Investigation of keyhole plume and molten pool based on a three-dimensional dynamic model with sharp interface formulation. *J. Phys. D: Appl. Phys.* 46, 055501 (2013).
5. Tan, W., Shin, Y.C.: Analysis of multi-phase interaction and its effects on keyhole dynamics with a multi-physics numerical model. *J. Phys. D: Appl. Phys.* 47, 345501 (2014).
6. Pang, S., *et al.*: 3D transient multiphase model for keyhole, vapor plume, and weld pool dynamics in laser welding including the ambient pressure effect. *Optics and Lasers in Engineering.* 74, 47–58 (2015).
7. Kouraytem, N., *et al.*: Effect of Laser-Matter Interaction on Molten Pool Flow and Keyhole Dynamics. *Phys. Rev. Applied.* 11, 064054 (2019).
8. Bayat, M., Mohanty, S., Hattel, J.H.: Multiphysics modelling of lack-of-fusion voids formation and evolution in IN718 made by multi-track/multi-layer L-PBF. *International Journal of Heat and Mass Transfer.* 139, 95–114 (2019).
9. Khairallah, S.A., *et al.*: Controlling interdependent meso-nanosecond dynamics and defect generation in metal 3D printing. *Science.* 368, 660–665 (2020).
10. Courtois, M., *et al.*: A complete model of keyhole and melt pool dynamics to analyze instabilities and collapse during laser welding. *Journal of Laser Applications.* 26, 042001 (2014).
11. Tomashchuk, *et al.*: Multiphysical Modeling of Keyhole Formation During Dissimilar Laser Welding. In: *Proceedings of the 2016 COMSOL Conference in Munich* (2016)
12. Bruyere, V., *et al.*: Multiphysics modeling of pulsed laser welding. *Journal of Laser Applications.* 29, 022403 (2017).
13. Gouffé, A.: Corrections d’ouverture des corps noirs artificiels compte tenu des diffusions multiples internes. *Revue d’optique.* 24, 1–10 (1945)
14. Mayi, Y.A., *et al.*: Laser-induced plume investigated by finite element modelling and scaling of particle entrainment in laser powder bed fusion. *J. Phys. D: Appl. Phys.* 53, 075306 (2020).
15. Steen, W.M., Mazumder, J.: *Laser Material Processing.* Springer London, London (2010)
16. Fabbro, R.: Depth Dependence and Keyhole Stability at Threshold, for Different Laser Welding Regimes. *Applied Sciences.* 10, 1487 (2020).
17. Mayi, Y.A., *et al.*: Two-Phase Flow Modelling of Metal Vaporisation under Static Laser Shot using a Double Domain ALE Method – A Feasibility Study. In: *Proceedings of the 2018 COMSOL Conference in Lausanne* (2018)
18. Mas, C.: *Modélisation physique du procédé de découpe de métaux par laser* (2003)
19. COMSOL Multiphysics® v 5.5. COMSOL AB, Stockholm, Sweden (2020)
20. Mills, K.C.: *Recommended values of thermophysical properties for selected commercial alloys.* Woodhead, Cambridge (2002)
21. Johnson, P., Christy, R.: Optical constants of transition metals: Ti, V, Cr, Mn, Fe, Co, Ni, and Pd. *Phys. Rev. B.* 9, 5056–5070 (1974).
22. Dean, J.A., Lange, N.A. eds: *Lange’s handbook of chemistry.* McGraw-Hill, New York, NY (1999)
23. Zhou, K., Wei, B.: Determination of the thermophysical properties of liquid and solid Ti–6Al–4V alloy. *Appl. Phys. A.* 122, 248 (2016).
24. Cunningham, R., *et al.*: Keyhole threshold and morphology in laser melting revealed by ultrahigh-speed x-ray imaging. *Science.* 363, 849–852 (2019).
25. Ye, J., *et al.*: Energy Coupling Mechanisms and Scaling Behavior Associated with Laser Powder Bed Fusion Additive Manufacturing. *Adv. Eng. Mater.* 21, 1900185 (2019).